A Self-Assembled Multiphasic Thin Film as an Oxygen Electrode for Enhanced Durability in Reversible Solid Oxide Cells

Fjorelo Buzi[1], Kosova Kreka[1], Jose Santiso[2], Laetitia Rapenne[3], Zijie Sha[4], James O. Douglas[4], Francesco Chiabrera[1], Alex Morata[1], Monica Burriel[3], Stephen Skinner[4], Lucile Bernadet[1], Federico Baiutti[1,5*], Albert Tarancón[1,6*]

[1] Catalonia Institute for Energy Research (IREC), Jardins de Les Dones de Negre 1, Sant Adrià Besos, Barcelona, Spain

[2] Catalonia Institute for Nanoscience and Nanotechnology (ICN2), CSIC and BIST, Campus de la Universitat Autònoma de Barcelona (UAB), Bellaterra, Barcelona, Spain

[3] Univ. Grenoble Alpes, CNRS, Grenoble INP, LMGP, 38000 Grenoble, France

[4] Department of Materials, Imperial College London, Exhibition Road, London, UK

[5] Department of Materials Chemistry, National Institute of Chemistry, Hajdrihova 19, Ljubljana SI-1000, Slovenia

[6] Catalan Institution for Research and Advanced Studies (ICREA), Passeig Lluís Companys 23, Barcelona, Spain

ABSTRACT

The implementation of nanocomposite materials as electrode layers represents a potential turning point for next-generation of solid oxide cells in order to reduce the use of critical raw materials. However, the substitution of bulk electrode materials by thin films is still under debate especially due to the uncertainty about their performance and stability under operando conditions, which restricts their use in real applications. In this work, we propose a multiphase nanocomposite characterized by a highly disordered microstructure and high cationic intermixing as a result from thin-film self-assembly of a perovskite-based mixed ionic-electronic conductor (lanthanum strontium cobaltite) and a fluorite-based pure ionic conductor (samarium-doped ceria) as an oxygen electrode for reversible solid oxide cells. Electrochemical characterization shows remarkable oxygen reduction reaction (fuel cell mode) and oxygen evolution activity (electrolysis mode) in comparison with state-of-the-art bulk electrodes, combined with outstanding long-term stability at operational temperatures of 700 ºC. The disordered nanostructure was implemented as a standalone oxygen electrode on commercial anode-supported cells, resulting in high electrical output in fuel cell and electrolysis mode for active layer thicknesses of only 200 nm (>95% decrease in critical raw materials with respect to conventional cathodes). The cell was operated for over 300 hours displaying excellent stability. Our findings unlock the hidden potential of advanced thin-film technologies for obtaining high-performance disordered electrodes based on nanocomposite self-assembly combining long durability and minimized use of critical raw materials.

Keywords: thin films, nanocomposites, air electrodes, solid oxide cells, electrolysis

1. INTRODUCTION

Solid oxide cells (SOCs) have drawn considerable attention in recent years due to their high efficiency in reversibly converting chemical energy into electricity without CO_2 emissions. Decisive advances have been achieved by the scientific and technological communities in tackling key issues related to performance enhancement, durability, resistance to poisoning and stack design[1,2]. As SOC technology is nowadays approaching widespread implementation in commercial and industrial applications[3], however, important challenges remain. Among the different cell components, an important leap forward is required especially with respect to air electrode composition and architecture, where a sluggish oxygen exchange and oxide ion diffusion kinetics, alongside thermochemical compatibility issues with the electrolyte[4–7], sensitivity to contaminants poisoning[8,9] and degradation at elevated temperatures[10,11] represent important constrains. Suitable air electrodes are limited to a restricted class of materials presenting a sufficient activity-stability trade-off, i.e. mixed electronic-ionic conducting (MIEC) perovskites[12–14]. As the target operational temperature decreases (<800 ºC), the choice becomes almost exclusively confined to Co-based perovskites[15,16]. State-of-the-art air electrode architectures are specifically comprised of $La_{1-x}Sr_xCo_{1-y}Fe_yO_3$ (including y =0) -doped CeO_2 porous composites, with a thickness range of 20-50 μm[17,18]. Notably, the strong geolocalization of cobalt resources combined with its ever-growing demand by incumbent energy technologies including Li-ion batteries, poses a serious threat to the SOC ecosystem[19,20]. New strategies for the development of next-generation oxygen electrodes with high performance and minimized use of critical raw materials are therefore mandatory.

Despite many efforts, replacement of Co with more abundant elements (e.g. Cu, Ni, Fe, Mn) typically comes together with a reduction of the electrochemical activity and of the long-term stability[21–24]. An alternative approach is represented by the use of advanced fabrication routes for achieving new architectures and enhanced performance through nanoengineering. Maximization of the reaction area and, even more importantly, emergence of nanoscale effects such as enhanced activity at grain boundaries and interfaces have shown great potential for the realization of next-generation optimized air electrodes[25–30]. In this context, thin film technologies assume relevance for tailoring functionalities via nanoengineering while maximizing materials utilization. Record values of electrochemical activity for air electrodes have been achieved this way[31,32]. Yet, the long-term stability of thin-film oxygen electrodes has so far been an insurmountable obstacle against application in practical cells, owing to degradation phenomena such as cation interdiffusion, coarsening or surface segregation at high temperatures[33–35].

Recently, self-assembly has come to the fore as a powerful approach for obtaining novel nanostructures combining high performance and long-term stability[36]. In particular, vertically aligned nanostructures (VANs) have revealed surprising effects e.g. improved electric transport, induced magnetism and high catalytic activity[37,38]. In the context of electrochemical systems, enhanced ionic conductivity and ORR kinetics have been reported for long-range ordered VANs[39,40]. In particular, previous research also from our group has highlighted that the one-pot fabrication of such nanocomposites determines the formation of equilibrium mixed compositions with superior stability at SOC operating temperatures[41,42]. As a consequence, VANs have been proven effective as oxygen electrode/electrolyte interlayers in solid oxide cells, acting as adhesion layer and barrier layer to obtain improved cell performance in combination with traditional oxygen electrodes[43,44].

In the present contribution, we show that self-assembled composite thin films are able to overcome typical stability limitations of nanostructures and can be directly employed as highly active oxygen electrode for stable operation in solid oxide cells. We do so by investigating the structural and electrochemical properties of a nominal $La_{0.6}Sr_{0.4}CoO_{3-\delta}$ (LSC)-$Ce_{0.8}Sm_{0.2}O_{2-\delta}$ (SDC) nanocomposite. Here, self-driven cation intermixing during fabrication leads to profound deviation from the nominal phase stoichiometry, as retrieved by a suite of advanced techniques including automatic crystallographic indexing and orientation/phase mapping (ASTAR) and atom probe tomography (APT). The resulting highly disordered nanostructure, which fits within the standard definition of high entropy oxides, possesses a unique combination of high electrochemical activity (area-specific resistance $\approx 10\ \Omega \cdot cm^{-2}$ at 500 ºC under anodic polarization) and thermochemical stability under SOC conditions. We demonstrate the straight applicability of the nanostructure as a standalone reversible oxygen electrode on commercial half cells (power density $>0.3\ W \cdot cm^{-2}$ in fuel cell mode, current density $0.6\ A \cdot cm^{-2}$ at 1.4 V in electrolysis mode at 700 ºC) and we show that high stability is achieved during continuous operation (ca. 320 hours in fuel cell mode and 100 hours in electrolysis mode).

2. RESULTS AND DISCUSSION

2.1 Structural and electrochemical characterization of LSC-SDC films

We first focus our attention on the fundamental structural and electrochemical properties of our LSC-SDC films. To this end, we analyze model films fabricated on top of single crystal YSZ substrates. The results of a global structural characterization are reported in **Figure 1**.

The LSC-SDC film quality after deposition is evaluated with a top-view AFM micrograph, shown in **Figure 1a,** highlighting a dense nanostructure with average grain size of around 30 nm and mean roughness of 4.5 nm. A structural analysis on the as-deposited material was performed by high-resolution XRD (**Figure 1b)**. The pattern displays the presence of perovskite and

fluorite peaks attributed to LSC and SDC (cubic or pseudocubic), respectively, with preferential (00l) orientation. Note that the SDC signal may originate from both the barrier layer and from SDC in the nanocomposite layer. The peak splitting at around 68.5º and 115º may be explained by the presence of additional (hk0)-oriented LSC, whose lattice spacing closely matches SDC (00l). An extra peak at ≈61º is attributed to a (220) peak from secondary phase cobalt oxide (CoO). It is important to emphasize that in the same angular regions the two couples of peaks are also maintained in the XRD pattern of LSC-SDC after 100 hours ageing at 700 ºC, i.e. no structural evolution occurs during the thermal ageing treatment (cf. **Supporting Fig. 3**). The calculated lattice parameter for LSC is 3.65 Å, with deviation from the bulk of 4.5%[45]. We ascribe such a deformation mainly to stoichiometric deviations resulting from cationic intermixing during fabrication, in agreement with our previous work and as demonstrated by APT analysis (see later in the text)[41]. In **Figure 1c** and **Figure 1d** the reciprocal space map and pole figures for LSC-SDC are shown, respectively, confirming the mixed orientation of the perovskite growing in a cube-on-cube (00l) arrangement and (hk0) configuration. A dedicated interpretation of these images is further discussed in **Supporting Note 1**.

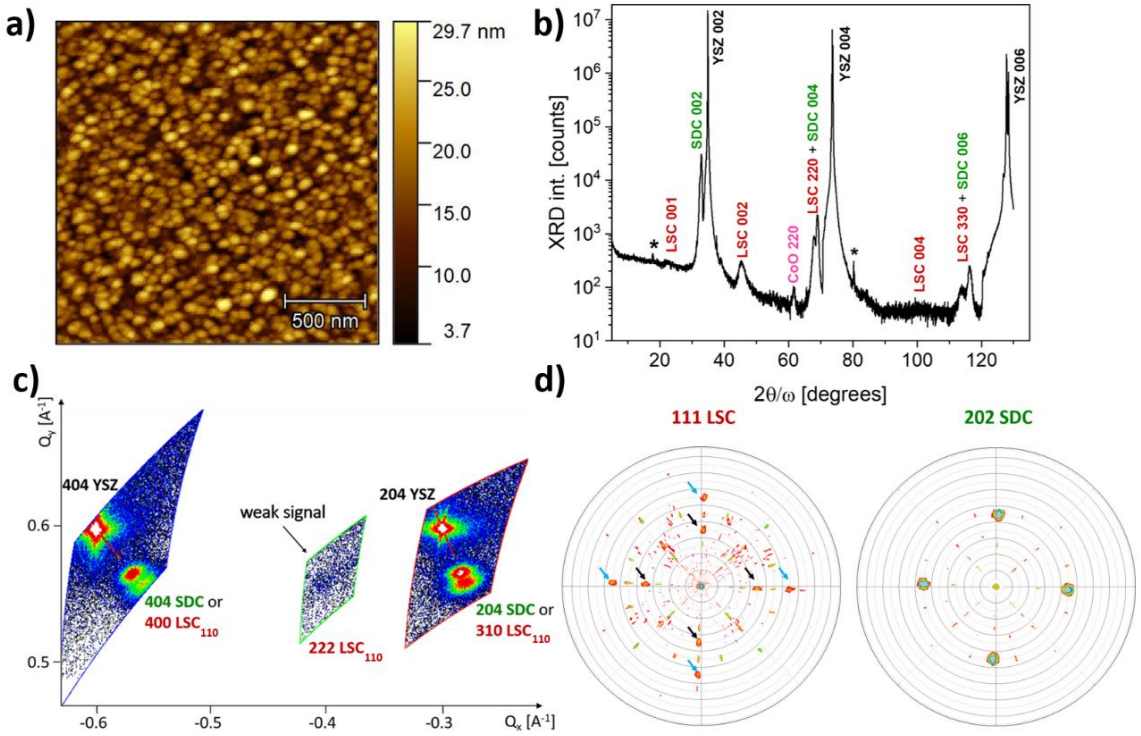

Figure 1. (a) Top-view AFM micrograph of LSC-SDC (R_{ms} =4.5 nm). **(b)** Two theta-omega scan by high resolution XRD for LSC-SDC. An additional peak attributed to CoO is shown. Reference patterns are used for identification of each phase: LSC (lattice parameter a_{LSC} = 3.82 Å[45]), SDC (a_{SDC}= 5.43 Å[46]), YSZ (a_{YSZ} = 5.14 Å[47]) and CoO (a_{CoO}= 4.26 Å[48]). Signals indicated by asterisks are attributed to artifact of instrumental origin. **(c)** RSM of (001)-oriented SDC domains (404 and 204 reflections) and (110)-oriented LSC domains (400, 222 and 310

reflections). 404 and 204 reflections from the YSZ substrate are visible as well. **(d)** Pole figure of the unique 111 reflection of LSC and 202 reflection of SDC. In the 111 LSC pole figure light blue arrows indicate 001-oriented reflections while black arrows indicate 110-oriented reflections and in the 202 SDC pole figure 001-oriented reflections only are visible indicating a cube-on-cube arrangement.

In **Figure 2a**, we report a cross-sectional HR-TEM micrograph of the LSC-SDC nanocomposite. The SDC buffer layer shows good crystallinity with a perfect epitaxial growth, as expected due to the YSZ substrate and the doped-ceria layer having same crystal structure and similar lattice parameters[46,47]. The LSC-SDC layer, instead, exhibits stacking faults and dislocations and does not give proof of a long-range ordered nanostructure. STEM and EDX images from **Figure 2b** bring into evidence other structural features as V-shaped domains penetrating the dense cross-section and extending to the interface with the barrier layer. The EDX maps displaying elemental distribution of cations in LSC, SDC and YSZ allow to identify such regions as Co-rich (cf. Fig. 2b). Across the rest of the film all elements appear to be distributed, i.e. an intimate phase intermixing is present in the nanocomposite layer. The higher Ce and Sm concentration that can be seen directly on top of the electrolyte corresponds to the SDC thin interlayer. HR-TEM and STEM-EDX maps for LSC-SDC after thermal ageing can be found in supplementary information, highlighting retained compositional features (see **Supporting Fig. 4a-b**). In order to improve the inherent spatial resolution, the structural properties of the films were also investigated by automated crystal phase and orientation mapping (ACOM) with a precession system (ASTAR). In **Figure 2c** and **Figure 2d** phase and orientation maps obtained from ASTAR characterization for as deposited LSC-SDC are depicted, respectively. In the phase distribution, nominal SDC appears as the main component with LSC occupying smaller regions. Such distribution can be explained with a preferential growth of the fluorite phase on top of the YSZ/SDC bilayer. We could also identify, with good phase index and reliability, small isolated regions of CoO_x, cf. Fig. 2b. Notably, the presence of isolated CoO_x clusters is in line with parallel investigation of Ishii et al. on the LSC-SDC system, where a certain tendency of LSC to partially decompose into highly active Co-rich binary oxides was highlighted[49]. The orientation maps validate the different orientations for the perovskite phase fraction, as discussed in the XRD section. Both SDC and LSC grow with preferential (001)-orientation, with LSC presenting a minority of (110)-oriented grains. Phase and orientation maps for the aged sample can be found in **Supporting Fig. 4c-d**, exhibiting similar characteristics.

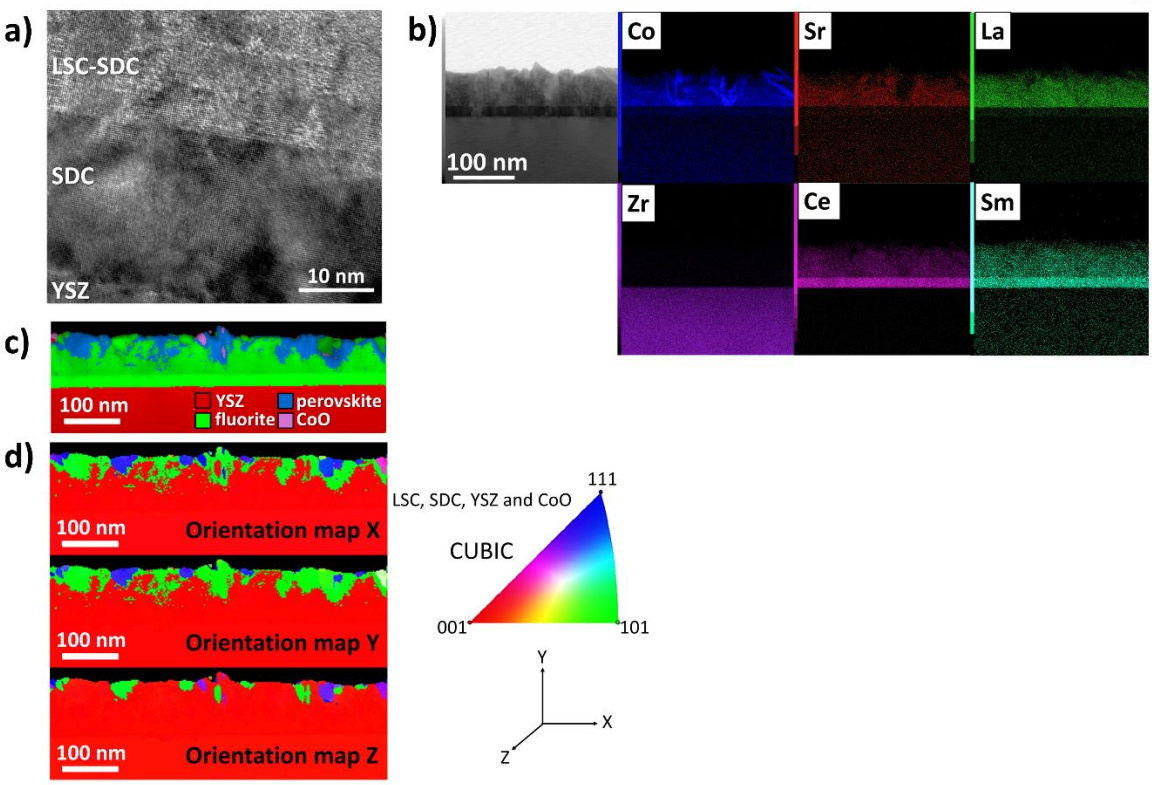

Figure 2. (a) TEM image of LSC-SDC nanocomposite highlighting mixed LSC and SDC phases in a disordered configuration. **(b)** STEM image and EDX mapping for elemental distribution across the film. **(c)** ASTAR phase and index maps of LSC-SDC nanocomposite with LSC phase shown in blue, SDC phase in green, YSZ substrate in red and particles of CoO detected in purple. **(d)** Orientation maps for each direction of LSC-SDC with a scheme of the color attribution and axis directions.

Owing to the close phase index values as well as to the very small domain size, TEM and ASTAR analyses present limitations in phase identification. To complement structural information with a detailed compositional mapping at the nanoscale level, APT characterization was therefore employed due to its unique sub-nanometer 3D spatial resolution[50]. **Figure 3a** shows the cationic spatial distribution considering all elements of interest (Co, Sr, La, Ce, Sm) for an APT conical tip extracted from a 200 nm-thick LSC-SDC sample on top of an SDC-buffered YSZ substrate. Cationic intermixing, as anticipated by the EDX imaging, is confirmed here, and thanks to the 3D resolution one can clearly identify the spatial phase distribution with isolated domains of high Co and Sr concentration. Conversely, La, Ce and Sm appear as homogeneously distributed. These findings offer insightful complementary information with respect to XRD and TEM: the perovskite phase, identified by APT as the areas that are rich in Co, Sr and lanthanides are characterized by a strong deviation from the nominal stoichiometry. The A-site in particular presents a high level of cationic intermixing due to the presence of La, Ce, Sr and Sm ions. This effect is compensated mainly by La migration into the complementary

phase, i.e. the Co-free fluorite matrix. The observed chemical intermixing also explains the cell deformation measured by XRD (cf. Fig. 1). In **Figure 3b** (horizontal projection)**-c** (vertical projection), Co and Sr isoconcentration surfaces are illustrated (respectively 28 at. % and 15 at. %). Beside the volumes of Sr and Co overlap (perovskite), one can notice a few isolated Co-rich regions only, which are ascribed to CoO_x secondary phases in agreement with the XRD analysis. The out-of-plane integrated linescans along two representative regions of interest (cf. Fig. 3c) shown in **Figure 3d** and **Figure 3e** confirm the alternation of Co+Sr and Ce signals, while La and Sm fraction show a largely flat profile as well as the presence of Co-rich domains, respectively. The highly disordered nanostructure of our LSC-SDC nanocomposite is substantially different from widely reported self-assembled ordered VANs (including $La_{0.5}Sr_{0.5}CoO_3$-$Ce_{0.8}Gd_{0.2}O_2$)[41,43,51], although it is similar to the results of a previous investigation lead by our group on the SDC-(La,Sr)(Mn,Cr)O_3 structure[42]. We ascribe such a finding to different film-substrate interactions (e.g. wettability) of the YSZ here employed opposite to more commonly employed model substrates (e.g. $SrTiO_3$), as well as to a certain chemical incompatibility between LSC and SDC during fabrication[49]. Notably, the lack of substrate/film coherence anticipates an easier integrability onto technological substrates (i.e. anode-supported solid oxide cells), as we detail next.

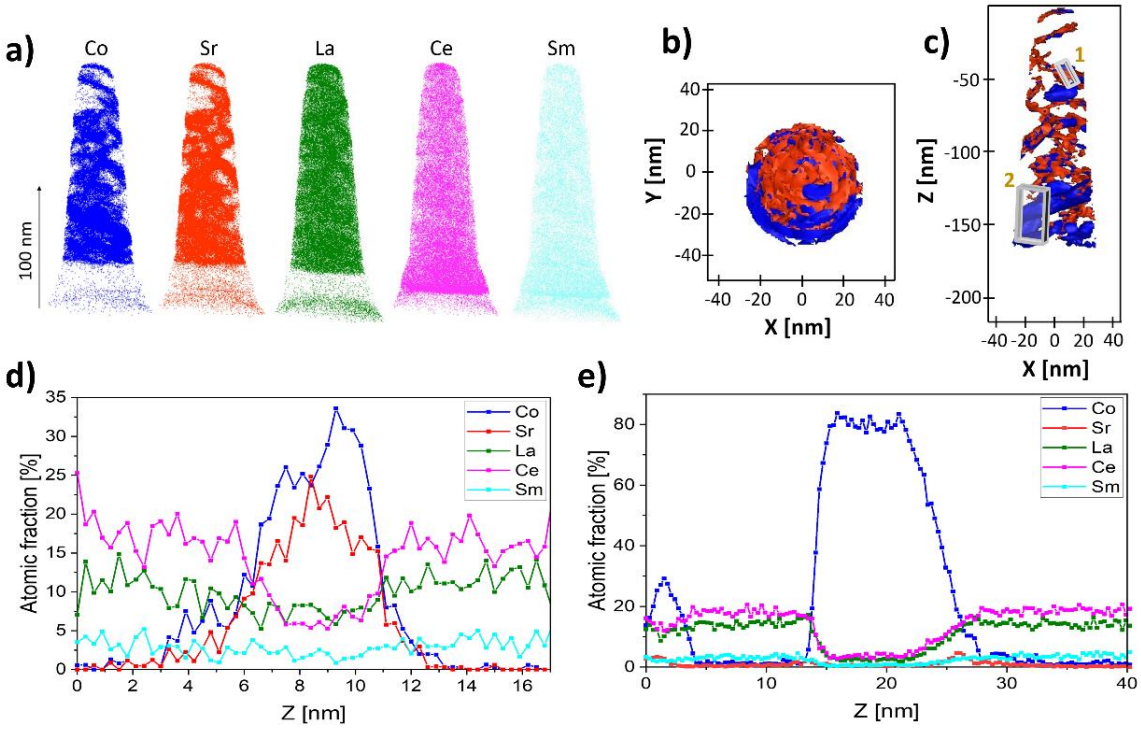

Figure 3. (a) Atom spatial distribution in the nanocomposite LSC-SDC film. **(b)** top-view and **(c)** lateral 3D view highlighting Co and Sr distribution in the film using 28 at.% and 15 at.%

isoconcentration surfaces respectively. **(d)** Atomic fraction along the region of interest 1 and **(e)** in the region of interest 2, both highlighted in image c.

The specific electrochemical performance of the LSC-SDC nanocomposite was first evaluated for the material on top of single crystal YSZ, in comparison with state-of-the-art single phase LSC dense films with the same nominal Sr doping. In **Figure 4a,** representative Nyquist plots of LSC-SDC and LSC recorded in open-circuit voltage in symmetric configuration with synthetic air and porous gold for current collection are presented. Along with the experimental data, fitting curves (continuous lines) are obtained from the application of a simple equivalent circuit (series of 2 RCPE elements) for the extraction of the total area-specific resistance (ASR). Please refer to **Supporting Note 2** for the physical interpretation of the impedance spectra. LSC shows low area-specific polarization resistance of 0.28 $\Omega \cdot cm^2$ at 700 ºC in air, in line with previous reports[52]. Nanocomposite LSC-SDC exhibits a higher surface resistance of 1.23 $\Omega \cdot cm^2$ at the same temperature and atmosphere. Fitted parameters and capacitance values extrapolated are summarized in the **Supporting Tables 1,2**. A temperature-dependent Arrhenius plot for both films in the 700 – 600 ºC temperature range is illustrated in **Figure 4b**, highlighting the comparison with $La_{0.8}Sr_{0.2}CoO_{3-\delta}$, (LSC82) and LSM-SDC VAN[41]. One can observe that LSC-SDC and LSC possess the lowest ASR values and activation energies (1.49 and 1.35 eV, respectively). When comparing our disordered nanocomposite with the ordered LSM-SDC VAN we notice a difference of around one order of magnitude in the same range of temperatures, with the nanocomposite proposed in this work holding the lowest polarization resistance. OCV measurements are however not representative of real SOC working conditions. To this end, we present in **Figure 4c** results on off-equilibrium area-specific resistance measurements obtained under polarization[53] (c.f. **Supporting Fig. 5** for Nyquist plots). Under these conditions, only one reaction governs the kinetics. Moreover, polarization drives changes in the bulk and surface defect concentration. For MIECs one expects an increase of oxygen vacancy concentration and decrease of electron holes at negative bias (cathodic polarization) in the bulk, while an opposite effect is experienced when changing the polarization direction i.e. positive bias (anodic polarization)[12]. Surface stoichiometry is affected as well, with segregation of different defect species (e.g. oxygen vacancies and Sr dopant), as well as possible formation of secondary phases[54]. In LSC, both anodic and cathodic polarization lead to electrode activation, as reported in literature and confirmed by our experimental observations[12]. Remarkably however, while under negative bias (i.e. fuel cell mode) LSC exhibits faster ORR kinetics than LSC-SDC, the situation is reversed for anodic bias (η >0.05 V – electrolysis mode), with LSC-SDC outperforming LSC for OER (up to 65% improvement for η = 0.15 V). We tentatively ascribe such an effect to an increased oxide ion diffusivity at high potentials through the acceptor-doped

ceria phase, while oxygen diffusion in LSC is slowed down by the decreased oxygen vacancy concentration[55].

A key parameter for the evaluation of an oxygen electrode performance is represented by the long-term thermal stability. This becomes especially critical in the case of thin films and heterostructures, in which, owing to the short distances involved, cation migration/interdiffusion may have a severe impact. In the case of LSC, Sr segregation phenomena have been shown to lead to dramatic degradation of the electrochemical activity[56]. We tested therefore the thermal stability of the LSC-SDC heterostructure by tracking the ASR during a thermal treatment of 100 hours at 700 ºC. The results are reported in **Figure 4d** and **Supporting Fig. 6**, in comparison with LSC. The strong degradation of the single-phase compound is apparent, with over 100% ASR increase during the course of the experiment (from 0.28 up to 0.58 $\Omega \cdot cm^2$). On the other hand, our nanocomposite shows outstanding thermal stability, with an initial strong decrease of ASR during the first ≈20 hours (-25%), followed by reduced degradation (+10%). Overall, we observed a ≈15% decrease of the ASR during the thermal ageing test (from 1.23 to 1.05 $\Omega \cdot cm^2$). Interestingly as reported in **Supporting Note 3**, a dedicated surface analysis by XPS, AFM and SEM (**Supporting Fig. 7-10** and **Supporting Tables 3,4**) highlights a similar evolution of the cationic ratios for LSC and LSC-SDC upon thermal ageing and especially an increase in the surface Sr content. Therefore, rather than just having a Sr-blocking effect in LSC[33,39], the rationalization of the observed thermal stability tentatively needs to take into account additional factors, e.g. an active role of ceria and of the CoO_x precipitates in the oxygen exchange[49,54]. We attribute a crucial role in the long-term stability also to the highly entropic environment experienced by our film as confirmed with compositional characterizations (e.g. STEM-EDX, APT) discussed previously. Various works ascribe such thermal and electrochemical resilience to cations intermixing in the perovskite lattice for air electrodes[57,58].

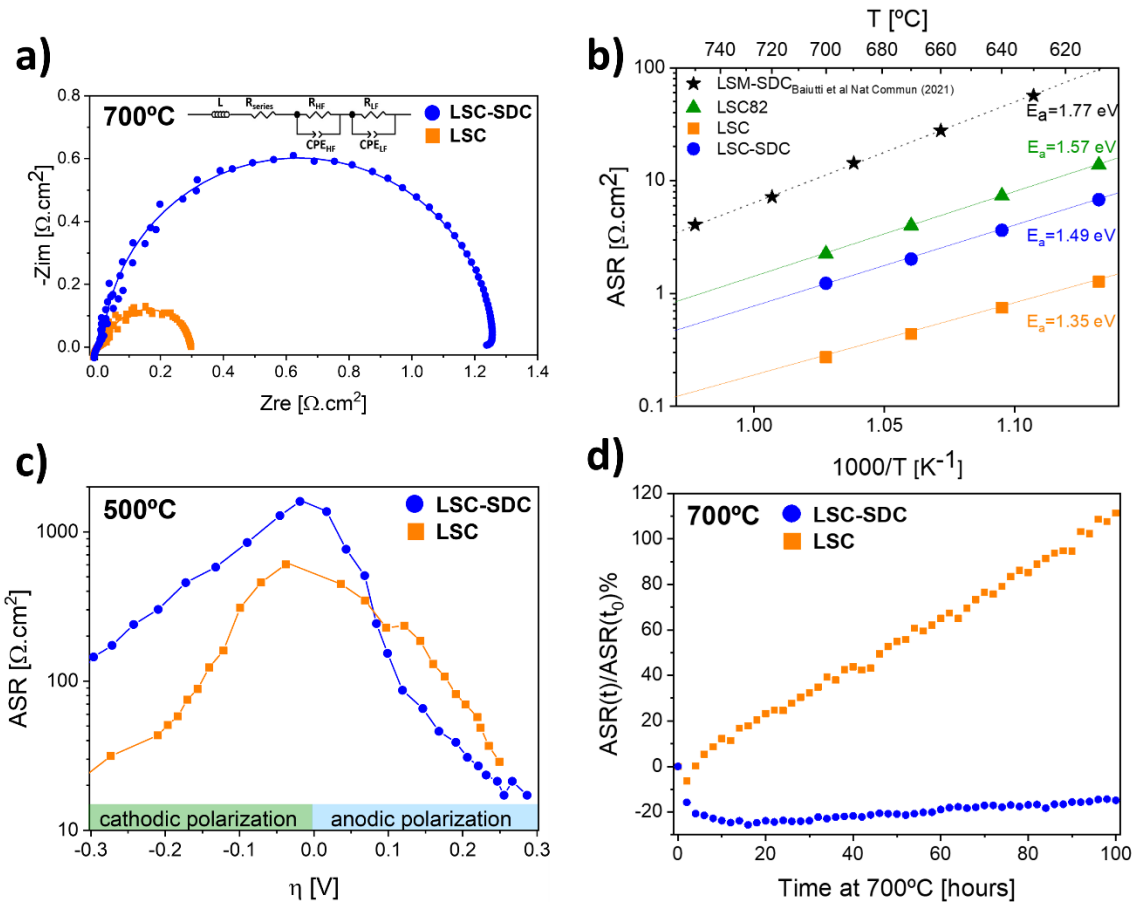

Figure 4. Impedance data of the studied materials from measurements performed under synthetic air. **(a)** Nyquist plots of LSC-SDC nanocomposite (blue) and LSC single phase (orange) at 700 ºC. **(b)** Arrhenius plot of the area-specific polarization resistance (ASR) as a function of temperature, and comparison with literature values for $La_{0.8}Sr_{0.2}CoO_{3-\delta}$, (LSC82) and LSM-SDC VAN[41]. **(c)** ASR vs overpotential curves for LSC-SDC nanocomposite (blue) and LSC single phase (orange) at 500 ºC under cathodic and anodic polarization. **(d)** ASR(t)/ASR(t_0)% vs time for LSC-SDC nanocomposite (blue) and LSC single phase (orange) during ageing treatment at 700 ºC.

2.2 Implementation of a full LSC-SDC thin-film as an oxygen electrode in SOC device

The results of the fundamental electrochemical characterization (cf. Fig. 4) point out the high potential of self-assembled LSC-SDC as an oxygen electrode, showing high activity in both cathodic (SOFC mode) and anodic (SOEC mode) conditions, as well as an outstanding thermochemical stability. Its direct applicability as an air electrode for real application in a reversible solid oxide cell was therefore tested. A 400 nm-thick bilayer composed by 200 nm of SDC barrier layer and 200 nm of LSC-SDC was deposited on top of a commercial Ni-YSZ-supported half-cell. Critically, while catalytically active current collectors (e.g. porous LSC or Pt) are typically employed, in our case inert porous Au was used, ensuring that the observed electrode performance is solely deriving from the ultrathin nanostructured layer. **Figure 5a** (low

magnification cross-sectional SEM) highlights the drastic volume minimization of the nanostructured air electrode enabled by our approach. We estimate a 95-99% decrease in the used material in comparison to SoA oxygen electrodes, which assumes relevance especially in consideration of the use of critical raw materials (La, Sr, Co). **Figure 5b** (high-magnification SEM) confirms the homogenous coverage and full density of the films. Note that the SEM analysis was carried out at the end of the long-term electrochemical test (see the text below). The characterization carried out with AFM and XRD (**Supporting Fig. 11)** confirms the straightforward integrability of the layer on technological supports (commercial button cells) as the main morphological and structural features of the LSC-SCD layer are maintained, namely phase separation, polycrystalline nature, and high surface quality.

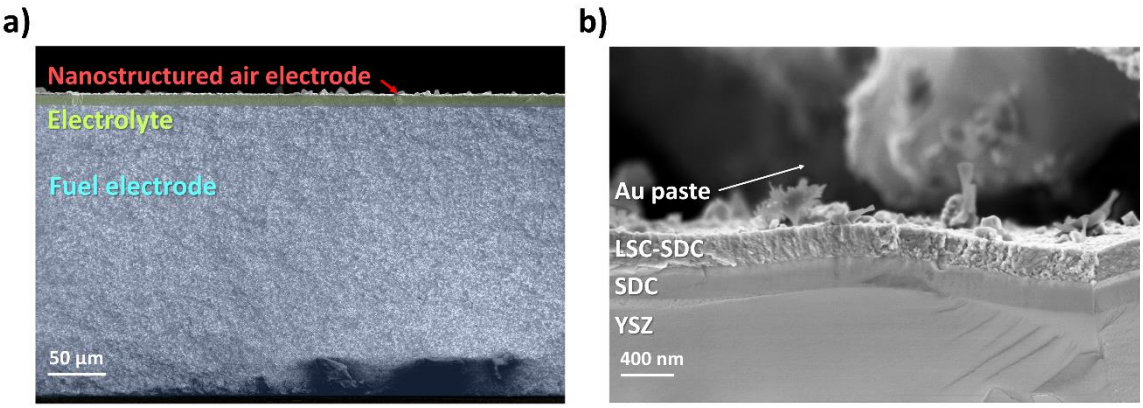

Figure 5. Cross-section SEM images of anode supported cell with nanostructured air electrode (post-mortem). (a) Low-magnification micrograph highlighting the thickness proportion of the thin-film based air electrode (red) in comparison with the fuel electrode (light-blue) and electrolyte (green). (b) Detail at high magnification on the SDC barrier layer and LSC-SDC active layer deposited by pulsed laser deposition.

In **Figure 6a,** current density-voltage and power density-voltage curves for the cell at 700 ºC in FC conditions under dry H_2 and synthetic air flow are shown (representative Nyquist plots in the inset – cf. **Supporting Table 5** for fitting details). A remarkable power value of 310 mW · cm^{-2} at 0.6 V is achieved. The low serial resistance contribution (≈0.15 Ω.cm^2) also indicates the perfect attachment of the PLD-produced oxygen electrode layer even without a post-fabrication annealing[59,60]. Operation under electrolysis conditions using a 50/50 mix of H_2/H_2O as a fuel and synthetic air at 700 ºC is illustrated in **Figure 6b** (Nyquist plots in the inset). The cell operates at a current density of 0.59 A · cm^{-2} at 1.4 V. **Figure 6c** and **Figure 6d** provide a direct comparison of the obtained performance with SoA cells in FC and EC conditions, respectively. The comparison is carried out in consideration of the estimated CRM mass units of the oxygen electrodes. The power output per unit mass in fuel cell operation mode achieved by the cell with the nanocomposite cathode, (Fig. 6c) is ca. 2 orders of magnitude higher than commercial cells using both bulky composite and single-phase cathodes based on the perovskite composition

$RE_{1-x}Sr_xCo_{1-y}Fe_yO_3$ (RE: rare-earth element; including y =0). A comparison with cells using PLD-deposited thin films is also reported[61,62]. Similarly, the electrolysis current per unit mass (cf. Fig. 6d) is up to 1.5 orders of magnitude higher than SoA cells. **Supporting Fig. 12** reports a direct comparison between the LSC-SDC based cell and another cell with thin film LSC as an air electrode. The results indicate similarity with the behaviour observed for the two films under applied bias (cf. Fig. 4c), with the LSC-SDC cell outperforming the LSC-based cell in SOEC conditions (+25% current density at 1.4 V). Comparable behaviour is instead obtained in SOFC mode, with good overlapping of the two i-V curves.

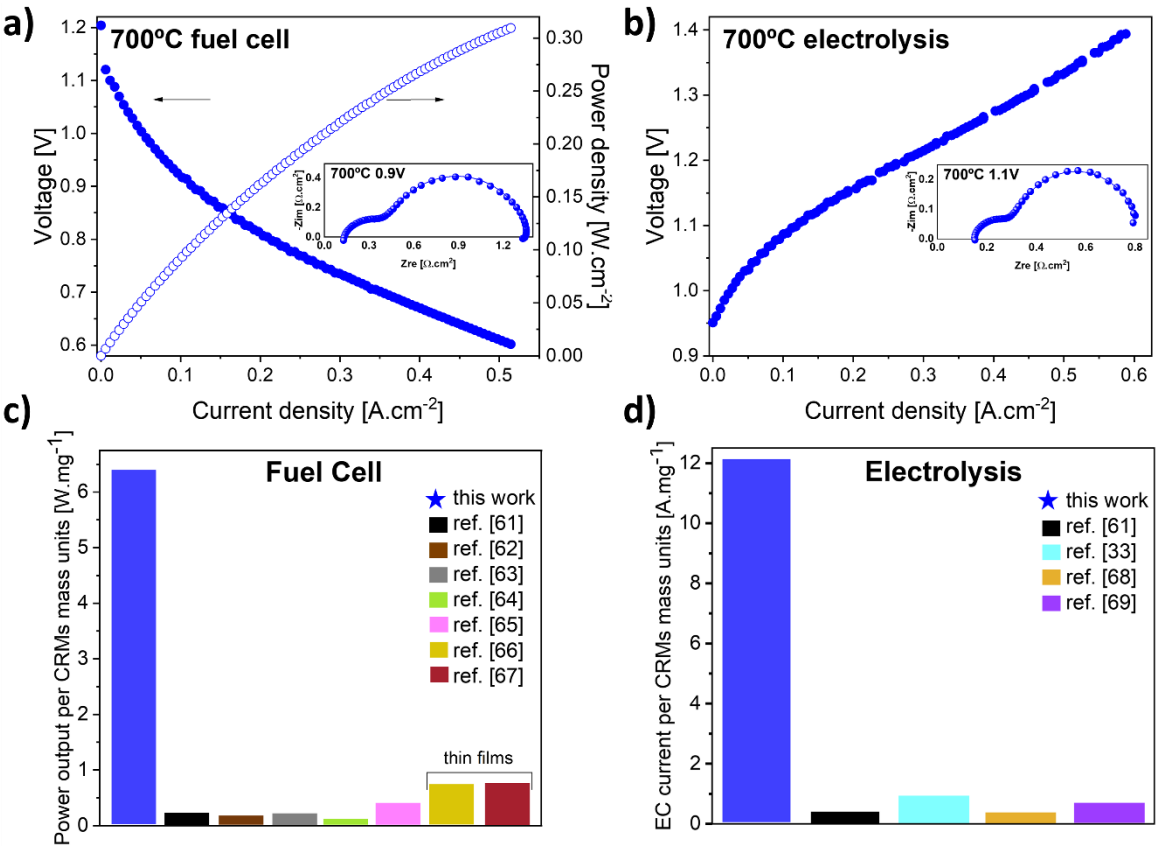

Figure 6. i-V and i-P curves for SDC + LSC-SDC bilayer on Ni-YSZ-supported cell at 700 ºC in SOFC **(a)** and SOEC mode **(b)** with insets showing representative Nyquist plots recorded at 0.9 V in fuel cell mode and 1.1 V in electrolysis mode. Gas flows during SOFC measurements were equal to 56 mL · min^{-1} · cm^{-2} of H_2 at the fuel electrode and 140 mL · min^{-1} · cm^{-2} of synthetic air at the oxygen electrode; while SOEC measurements were performed with a gas flows of 22 mL · min^{-1} · cm^{-2} for both H_2 and H_2O equivalent to a 50/50 H_2/H_2O fuel composition at the fuel electrode and 112 mL · min^{-1} · cm^{-2} of synthetic air at the oxygen electrode. Comparison of the power output in SOFC mode **(c)** or electrolysis current in SOEC mode **(d)** per critical raw materials mass units of the cell in this work with state-of-the-art cells[33,61–69].

Finally, a long-term degradation test in SOFC galvanostatic mode (0.20 A · cm^{-2}) at 700 ºC under dry H_2 and synthetic air was performed. As shown in **Figure** 7**a**, the initial voltage of 0.8 V experiences an initial drop of ca. 20-25 mV during the first 50 hours and a stable behaviour afterwards. A linear degradation of 33.3 mV · kh^{-1} (4.3% kh^{-1}) was observed according to the galvanostatic test. The i-V curves during degradation (**Supporting Fig. 13a**) confirm the findings, showing an initial slight drop in performance (≈50 hours) followed by stable behaviour for ca. 300 hours). A SOEC degradation test in galvanostatic mode (0.15 A · cm^{-2}) at 700 ºC under H_2/H_2O (50/50) and synthetic air was also performed as depicted in **Figure 7b** with related i-V curves presented in **Supporting Fig. 13b**. The slight difference in electrochemical performances (cf. Fig. 6b) are to be ascribed to sample-to-sample variability. A 100-hours operation test under SOEC conditions was carried out, revealing a degradation rate of ca. 11.2% kh^{-1} after an initial voltage increase of ca. 130-135 mV in the first ≈40 hours. Although the observed degradation is generally higher than SoA cells, for which values <1 kh^{-1} are targeted and now being reported[70], such a stability at high temperatures and during operation is unprecedented for a thin-film nanostructure. In this regard, Shin et al. studied the properties of a fuel cell with an ultrathin atomic layer deposited CeO_2 cathode overlayer, demonstrating limited stability already after 10 hours of operation[32]. Lee et al. reported on a solid oxide fuel cell a sputtered LSCF-YSZ composite cathodes with continuous operation for 7 hours only[34]. Develos-Bagarinao et al. demonstrated the integration of a PLD nanoengineered cathode on a commercial cell showing high performance (2.5 A · cm^{-2} at 600 ºC) but dramatic degradation (over 50% performance loss) over 250 hours of operation[35]. To the best of our knowledge, our results prove for the first time the long-term operation of a nanostructured thin-film cathode alone (i.e. without additional catalytic layers) in a full solid oxide cell, with very limited loss of performance and no apparent structural evolution. Nonetheless, stable long-term operation on thin-film level can be found in literature, including PLD-produced LSC single-phase air electrodes, however, such films are at least 1 order of magnitude thicker (> 2 µm) than our film and stability tests are performed at lower temperatures (<600 ºC). Kim et al. show LSC stability on a full cell only for 70 hours at 550 ºC[61], while Shin et al. implemented a 3-µm thick LSC layer on a large-area cell operating for longer time at 500 ºC but without proofs of long-term performances in electrolysis mode[62]. At the end of the test, the LSC-SDC layer maintains full density and conformality throughout the whole cross-section with no specific alteration (cf. Fig. 5).

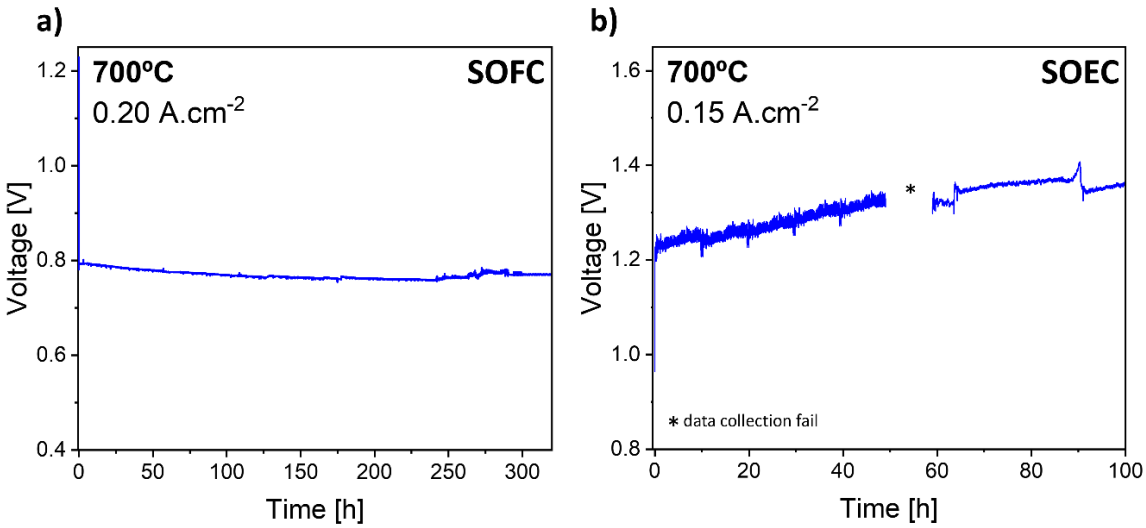

Figure 7. (a) Durability test of SDC + LSC-SDC bilayer on Ni-YSZ-supported cells for over 300 hours at 700 ºC under 0.20 A.cm^{-2} cathodic polarization in SOFC mode and **(b)** for 100 hours at 700 ºC under 0.15 A.cm^{-2} anodic polarization in SOEC mode.

3. CONCLUSIONS

We presented a thin film LSC-SDC nanocomposite fabricated by PLD as an excellent air electrode for reversible operation in solid oxide cells. The electrode shows remarkable activity increase upon polarization along with good thermal resistance when tested on model substrates. Consequently, we prove for the first time that advanced thin-film technology can be implemented in full SOC devices for the fabrication of durable high-temperature electrodes (over 300 hours in fuel cell operation) with minimized thickness (200 nm), providing clear advantages in terms of material utilization in comparison to traditional manufacturing. We suggest that self-assembly, leading to the formation of isolated clusters comprising perovskite cobaltite and binary Co-rich oxides embedded in a ceria matrix, along with intimate cationic intermixing between the perovskite and the fluorite phases, yields an outstanding combination of high electrochemical activity and long-term stability.

4. EXPERIMENTAL SECTION

Thin Film Fabrication

Composite LSC-SDC and single phase LSC thin films were deposited in a large-area pulsed laser deposition equipment (PVD systems, PLD 5000) equipped with a 248 nm KrF excimer laser (Lambda Physics, COMpex PRO 205) on yttrium-stabilized zirconia YSZ (001) substrates (10 x 10 x 0.5 mm, Crystec GmbH) in an asymmetrical and symmetrical configuration for fundamental and electrochemical studies. LSC-SDC films were deposited at 800 ºC, while LSC films at 750 ºC; both films (≈100 nm thickness) were fabricated with 0.007 mbar oxygen

pressure, target-to-substrate distance of 90 mm, laser fluency ≈0.8 J · cm^{-2}, laser frequency 2 Hz for LSC-SDC and 10 Hz for LSC. A thin SDC layer (≈10 nm) was deposited at similar conditions at the oxygen electrode-electrolyte interface to avoid elemental intermixing with the YSZ substrate and secondary phase formation. Complete SOC cells were prepared to evaluate performances as well as durability in fuel cell (SOFC) and electrolysis (SOEC) modes. A bilayer of SDC/LSC-SDC having ≈200 nm of doped ceria as the barrier layer and ≈200 nm of LSC-SDC as the active material was produced. The deposition temperature was set at 750 ºC and the frequency at 10 Hz, while the rest of parameters were kept identical to the previous depositions on YSZ (001). Initially, 8YSZ tapes (20 mm diameter; 150 µm-thick, Kerafol) were used for deposition optimization and subsequentially, commercial state-of-the-art Ni-YSZ-supported half cells, comprising a thin electrolyte (≈8 µm-thick YSZ) supported by a Ni-YSZ substrate (≈250 µm-thick) with a 20 mm diameter were employed. The oxygen electrode active area on the half-cell is 1.77 cm^2. For the nanocomposite LSC-SDC a home-made target was prepared from commercial powders of $La_{0.6}Sr_{0.4}CoO_{3-\delta}$ and $Ce_{0.8}Sm0_{0.2}O_{2-\delta}$ (1:1 wt.%, Kceracell) via ball milling in ethanol solution. The dried powder mixture was uniaxially pressed (7 MPa, 30 s) to form a pellet of ≈2.5 cm in diameter. The pellet was sintered at 1300 ºC for 4 h (heating and cooling ramps 5 ºC/min). Commercial targets were used for LSC64 and SDC single-phase depositions. Please refer to **Supporting Fig. 1** for a schematic representation of the cells adopted in this work.

Microscopy and Structural Analysis

Atom force microscopy (AFM) and scanning electron microscopy (SEM) top-views and cross-sections were acquired with equipment provided by Park System Corp. and Zeiss, respectively. X-ray diffraction was performed on the films by using a X'Pert Pro MRD diffractometer from Malvern Panalytical. Experimental details include three optics: for the 2theta-omega scans a low-resolution primary optics with Cu Kα radiation (45 kV, 40 mA), a parabolic mirror and a Ni filter were used. Regarding the reciprocal space mapping, high resolution primary optics with a parabolic mirror plus a 2xGe(220) monochromator were adopted. Finally, for the texture analysis of the pole figures a primary optics with point focus Cu source and a capillary lens were employed. Transmission electron microscopy (TEM) and high-resolution transmission electron microscopy (HR-TEM) images were recorded with a JEOL JEM 2010 LaB6 microscope operating at 200 kV with a 0.19 nm point-to-point resolution. Energy-Dispersive X-ray Spectroscopy (EDX) mappings were collected by Scanning Transmission Electron Microscopy (STEM) with a JEOL 2100F FEG microscope operating at 200 kV with a 0.2 nm resolution in the scanning mode and equipped with a JEOL SDD Centurio detector with a large solid angle of up to 0.98 steradians. The local structural properties of the LSC-SDC nanocomposite were further investigated by using an automated crystal phase and orientation

mapping (ACOM) with a precession system (ASTAR) implemented in the JEOL 2100F FEG microscope. The crystal phase and orientation maps were obtained by precession of the primary electron beam around the microscope's optical axis at an angle of 1.2° while collecting the electron diffraction patterns at a rate of 100 frames/s with a step size of 2 nm.

Atom Probe Tomography (APT)

Atom probe tomography was applied to study the local elemental distribution of the LSC-SDC nanocomposite. The needle-shaped APT specimen (as illustrated in **Supporting Fig. 2**) was prepared through focused ion beam (FIB) milling and subsequent lift-out (Thermofisher Scientific Helios 5 CX DuelBeam microscope), with the surface sputter coated with a layer of Pt to prevent charging before FIB sample preparation. The APT measurements were carried out at 55 K using laser pulsing mode, with a laser energy of 10 pJ, a pulse frequency of 200 kHz, and a detection rate of 1% (Cameca LEAP 5000 XR atom probe microscope). The acquired data was analysed using the Cameca integrated visualization and analysis software (IVAS) within the AP suite 6.1 toolkit.

X-ray Photoelectron Spectroscopy (XPS)

XPS measurements were performed at room temperature with a SPECS PHOIBOS 150 hemispherical analyzer (SPECS GmbH, Berlin, Germany) in a base pressure of $5x10^{-10}$ mbar using monochromatic Al K alpha radiation (1486.74 eV) as excitation source operated at 300 W. The energy resolution as measured by the FWHM of the Ag 3d5/2 peak for a sputtered silver foil was 0.62 eV. All measurements were realized at take-off angle of 0º and 60º for different surface sensitivities and a flood gun was used during the analysis to compensate for charging effects on the samples.

Electrochemical Characterization

Electrochemical impedance measurements were carried out with a Novocontrol impedance spectrometer using a frequency sweep in the range of 1 MHz – 0.1 Hz, in open circuit potential and with an AC amplitude of 50 mV. Impedance spectra for materials study and thermal resistance tests were recorded on symmetric cells with films deposited on both sides of a single crystal YSZ substrate. Porous Au paste (Fuel Cell Materials) was brushed on each side for current collection. The films were exposed to oxidizing symmetric atmosphere using synthetic air flow. The samples were mounted in a ProboStat station (NorECs) placed in a vertical furnace. Ageing experiments were performed at 700 ºC for 100 h. An asymmetric cell configuration was also used for studies under bias performed in a Linkam700 where a 4-probe configuration was adopted. The counter electrode was made of porous silver while for the working electrode gold paste was painted on top for current collection. All measurements were

performed in oxidizing atmosphere and each of them consists of 2 min of chronoamperometry, where the current at an applied potential was monitored, followed by an impedance measurement where the AC voltage was set at 30 mV and the same DC potential was applied. The overpotential of the thin film electrode was then calculated using $\eta = (V_{applied} - I \times R)$ where R is the sum of the resistances associated to YSZ and porous Ag.

Complete SOC cells prepared on Ni-YSZ-supported cells were mounted in a similar ProboStat station with separate compartment on the bottom part for supplementary heating to prevent condensation of water steam during measurements. Ceramabond (Aremco) paste was applied to fix and seal the cells on top of the ProboStat system and separate air and fuel chambers. Au and Ni paste and meshes were used for current collection on the air and fuel electrode side, respectively. The measurements of the complete SOCs in fuel cell mode were done under dry H_2 fuel and synthetic air with flow densities of 56 and 140 mL · min^{-1} · cm^{-2} respectively. On the other hand, in electrolysis mode a 50/50 H_2/H_2O fuel composition mix was used with a flow of 22 mL · min^{-1} · cm^{-2} for each component of the fuel and 112 mL · min^{-1} · cm^{-2} for synthetic air. In both modes, all electrochemical characterizations of cells including impedance spectroscopy (EIS) and i-V curves were collected using a PARSTAT 2273 potentiostat, and for the long-term tests under bias an electronic load M9812 from Maynuo Electronic Co. Ltd. coupled with a power supply Velleman LABPS3005D were used.

AUTHOR INFORMATION

Corresponding Authors

Federico Baiutti − Department of Advanced Materials for Energy, Catalonia Institute for Energy Research (IREC), Barcelona 08930, Spain; Department of Materials Chemistry, National Institute of Chemistry, Ljubljana SI-1000, Slovenia; https://orcid.org/0000-0001-9664-2486; Email: fbaiutti@irec.cat

Albert Tarancón − Department of Advanced Materials for Energy, Catalonia Institute for Energy Research (IREC), Barcelona 08930, Spain; ICREA, 08010 Barcelona, Spain; https://orcid.org/0000-0002-1933-2406; Email: atarancon@irec.cat

Authors Contributions

Experiments were conceived by F. Buzi, F. Baiutti, L. Bernadet, F. Chiabrera, K. Kreka, A. Morata, A. Tarancón. Samples preparation was carried out by F. Buzi with morphological (AFM, SEM) and electrochemical characterizations by F. Buzi (materials study on YSZ single crystal and nanocomposite tests on Ni-YSZ button cells including long-term operations) and K. Kreka (chronoamperometry analysis on YSZ single crystal and characterization of LSC on Ni-

YSZ button cell for reference). High resolution XRD analysis and interpretation were performed by J. Santiso. TEM-EDX and ASTAR mappings and interpretation by L. Rapenne and M. Burriel. APT characterization and interpretation by Z. Sha with the support of J.O. Douglas and S. Skinner. F. Buzi curated the data and prepared the images and the text in the original draft. All the authors contributed to the interpretation and discussion of the experimental data and to the final editing of the original draft.

ACKNOWLEDGEMENTS

This project received funding from the European Union's Horizon 2020 research and innovation program under grant agreement No. 101017709 (EPISTORE), under the Government of Catalonia (2021 SGR 00750) and under the Marie Skłodowska-Curie grant agreement No. 840787 (Thin-CATALYzER). The authors acknowledge Jan Pieter Ouweltjes and Dario Montinaro (SolydEra S.p.A., Italy) for the half-cells supply employed in this work.

COFLICT OF INTEREST

The authors declare no conflict of interest.

REFERENCES

(1) Irvine, J. T. S.; Neagu, D.; Verbraeken, M. C.; Chatzichristodoulou, C.; Graves, C.; Mogensen, M. B. Evolution of the Electrochemical Interface in High-Temperature Fuel Cells and Electrolysers. *Nat. Energy* **2016**, *1* (1), 15014.

(2) Hauch, A.; Küngas, R.; Blennow, P.; Hansen, A. B.; Hansen, J. B.; Mathiesen, B. V.; Mogensen, M. B. Recent Advances in Solid Oxide Cell Technology for Electrolysis. *Science* **2020**, *370* (6513), eaba6118.

(3) Boldrin, P.; Brandon, N. P. Progress and Outlook for Solid Oxide Fuel Cells for Transportation Applications. *Nat. Catal.* **2019**, *2* (7), 571–577.

(4) Shin, J.-S.; Saqib, M.; Jo, M.; Park, K.; Park, K. M.; Ahn, J. S.; Lim, H.-T.; Park, J.-Y. Degradation Mechanisms of Solid Oxide Fuel Cells under Various Thermal Cycling Conditions. *ACS Appl. Mater. Interfaces* **2021**, *13* (42), 49868–49878.

(5) Wu, Y.; Xu, X.; Yan, Z.; Zhong, Z. Thermo-Electro-Chemo-Mechanical Modeling of Solid Oxide Fuel Cell for Stress and Failure Evolution during Duty Cycle. *J. Electrochem. Soc.* **2021**, *168* (4), 044511.

(6) Lim, Y.; Park, J.; Lee, H.; Ku, M.; Kim, Y.-B. Rapid Fabrication of Lanthanum Strontium Cobalt Ferrite (LSCF) with Suppression of LSCF/YSZ Chemical Side Reaction via Flash Light Sintering for SOFCs. *Nano Energy* **2021**, *90*, 106524.

(7) Sandoval, M. V.; Cárdenas, C.; Capoen, E.; Pirovano, C.; Roussel, P.; Gauthier, G. H. Performance of La0.5Sr1.5MnO4±δ Ruddlesden-Popper Manganite as Electrode Material for Symmetrical Solid Oxide Fuel Cells. Part A. The Oxygen Reduction Reaction. *Electrochimica Acta* **2019**, *304*, 415–427.

(8) Ni, N.; Wang, C. C.; Jiang, S. P.; Skinner, S. J. Synergistic Effects of Temperature and Polarization on Cr Poisoning of $La_{0.6}Sr_{0.4}Co_{0.2}Fe_{0.8}O_{3-\delta}$ Solid Oxide Fuel Cell Cathodes. *J. Mater. Chem. A* **2019**, *7* (15), 9253–9262.

(9) Riedl, C.; Siebenhofer, M.; Nenning, A.; Schmid, A.; Weiss, M.; Rameshan, C.; Limbeck, A.; Kubicek, M.; Opitz, A. K.; Fleig, J. *In Situ* Techniques Reveal the True Capabilities of SOFC Cathode Materials and Their Sudden Degradation Due to Omnipresent Sulfur Trace Impurities. *J. Mater. Chem. A* **2022**, *10* (28), 14838–14848.

(10) Lee, W.; Han, J. W.; Chen, Y.; Cai, Z.; Yildiz, B. Cation Size Mismatch and Charge Interactions Drive Dopant Segregation at the Surfaces of Manganite Perovskites. *J. Am. Chem. Soc.* **2013**, *135* (21), 7909–7925.

(11) Kim, D.; Bliem, R.; Hess, F.; Gallet, J.-J.; Yildiz, B. Electrochemical Polarization Dependence of the Elastic and Electrostatic Driving Forces to Aliovalent Dopant Segregation on $LaMnO_3$. *J. Am. Chem. Soc.* **2020**, *142* (7), 3548–3563.

(12) Siebenhofer, M.; Riedl, C.; Schmid, A.; Limbeck, A.; Opitz, A. K.; Fleig, J.; Kubicek, M. Investigating Oxygen Reduction Pathways on Pristine SOFC Cathode Surfaces by *in Situ* PLD Impedance Spectroscopy. *J. Mater. Chem. A* **2022**, *10* (5), 2305–2319.

(13) Yatoo, M. A.; Skinner, S. J. Ruddlesden-Popper Phase Materials for Solid Oxide Fuel Cell Cathodes: A Short Review. *Mater. Today Proc.* **2022**, *56*, 3747–3754.

(14) Tahir, N. N. M.; Baharuddin, N. A.; Samat, A. A.; Osman, N.; Somalu, M. R. A Review on Cathode Materials for Conventional and Proton-Conducting Solid Oxide Fuel Cells. *J. Alloys Compd.* **2022**, *894*, 162458.

(15) Shao, Z.; Haile, S. M. A High-Performance Cathode for the next Generation of Solid-Oxide Fuel Cells. **2004**, *431*.

(16) Celikbilek, O.; Thieu, C.-A.; Agnese, F.; Calì, E.; Lenser, C.; Menzler, N. H.; Son, J.-W.; Skinner, S. J.; Djurado, E. Enhanced Catalytic Activity of Nanostructured, A-Site Deficient $(La_{0.7}Sr_{0.3})_{0.95}(Co_{0.2}Fe_{0.8})O_{3-\delta}$ for SOFC Cathodes. *J. Mater. Chem. A* **2019**, *7* (43), 25102–25111.

(17) Park, J.-H.; Hong, W.-S.; Yoon, K. J.; Lee, J.-H.; Lee, H.-W.; Son, J.-W. Physical and Electrochemical Characteristics of Pulsed Laser Deposited $La_{0.6}Sr_{0.4}CoO_{3-\delta}$-$Ce_{0.9}Gd_{0.1}O_{2-\delta}$ Nanocomposites as a Function of the Mixing Ratio. *J. Electrochem. Soc.* **2014**, *161* (1), F16–F22.

(18) Kim, Y. T.; Shikazono, N. Evaluation of Electrochemical Reaction Mechanisms of La0.6Sr0.4CoO3-δ-Gd0.1Ce0.9O2-δ Composite Cathodes by 3D Numerical Simulation. *Solid State Ion.* **2018**, *319*, 162–169.

(19) Gent, W. E.; Busse, G. M.; House, K. Z. The Predicted Persistence of Cobalt in Lithium-Ion Batteries. *Nat. Energy* **2022**, *7* (12), 1132–1143.

(20) Pommeret, A.; Ricci, F.; Schubert, K. Critical Raw Materials for the Energy Transition. *Eur. Econ. Rev.* **2022**, *141*, 103991.

(21) Sun, C.; Hui, R.; Roller, J. Cathode Materials for Solid Oxide Fuel Cells: A Review. *J. Solid State Electrochem.* **2010**, *14* (7), 1125–1144.

(22) Carneiro, J. S. A.; Brocca, R. A.; Lucena, M. L. R. S.; Nikolla, E. Optimizing Cathode Materials for Intermediate-Temperature Solid Oxide Fuel Cells (SOFCs): Oxygen Reduction on Nanostructured Lanthanum Nickelate Oxides. *Appl. Catal. B Environ.* **2017**, *200*, 106–113.

(23) Niemczyk, A.; Du, Z.; Olszewska, A.; Marzec, M.; Gajewska, M.; Świerczek, K.; Zhao, H.; Poudel, B.; Dabrowski, B. Effective Oxygen Reduction on A-Site Substituted $LaCuO_{3-\delta}$: Toward Air Electrodes for SOFCs Based on Perovskite-Type Copper Oxides. *J. Mater. Chem. A* **2019**, *7* (48), 27403–27416.

(24) Cai, H.; Zhang, L.; Xu, J.; Huang, J.; Wei, X.; Wang, L.; Song, Z.; Long, W. Cobalt–Free La0.5Sr0.5Fe0.9Mo0.1O3– Electrode for Symmetrical SOFC Running on H2 and CO Fuels. *Electrochimica Acta* **2019**, *320*, 134642.

(25) Sanna, S.; Esposito, V.; Tebano, A.; Licoccia, S.; Traversa, E.; Balestrino, G. Enhancement of Ionic Conductivity in Sm-Doped Ceria/Yttria-Stabilized Zirconia Heteroepitaxial Structures. *Small* **2010**, *6* (17), 1863–1867.

(26) Benel, C.; Darbandi, A. J.; Djenadic, R.; Evans, A.; Tölke, R.; Prestat, M.; Hahn, H. Synthesis and Characterization of Nanoparticulate La0.6Sr0.4CoO3−δ Cathodes for Thin-Film Solid Oxide Fuel Cells. *J. Power Sources* **2013**, *229*, 258–264.

(27) Develos-Bagarinao, K.; Budiman, R. A.; Ishiyama, T.; Yamaji, K.; Kishimoto, H. Leveraging Catalytic Effects of Heterointerfaces through Multilayering for Superior Cathode Performance. *J. Power Sources* **2020**, *480*, 229094.

(28) Baiutti, F.; Chiabrera, F.; Diercks, D.; Cavallaro, A.; Yedra, L.; López-Conesa, L.; Estradé, S.; Peiró, F.; Morata, A.; Aguadero, A.; Tarancón, A. Direct Measurement of Oxygen Mass Transport at the Nanoscale. *Adv. Mater.* **2021**, *33* (48), 2105622.

(29) Chiabrera, F.; Baiutti, F.; Diercks, D.; Cavallaro, A.; Aguadero, A.; Morata, A.; Tarancón, A. Visualizing Local Fast Ionic Conduction Pathways in Nanocrystalline Lanthanum Manganite by Isotope Exchange-Atom Probe Tomography. *J. Mater. Chem. A* **2022**, *10* (5), 2228–2234.

(30) Thoréton, V.; Niania, M.; Druce, J.; Tellez, H.; Kilner, J. A. Oxygen Diffusion in Ceramic Mixed Conducting La $_{0.6}$ Sr $_{0.4}$ Co $_{0.2}$ Fe $_{0.8}$ O $_{3-\delta}$: The Role of Grain and Twin Boundaries. *J. Electrochem. Soc.* **2022**, *169* (4), 044513.

(31) Januschewsky, J.; Ahrens, M.; Opitz, A.; Kubel, F.; Fleig, J. Optimized La0.6Sr0.4CoO3–δ Thin-Film Electrodes with Extremely Fast Oxygen-Reduction Kinetics. *Adv. Funct. Mater.* **2009**, *19* (19), 3151–3156.

(32) Shin, J. W.; Oh, S.; Lee, S.; Yu, J.-G.; Park, J.; Go, D.; Yang, B. C.; Kim, H. J.; An, J. Ultrathin Atomic Layer-Deposited CeO $_2$ Overlayer for High-Performance Fuel Cell Electrodes. *ACS Appl. Mater. Interfaces* **2019**, *11* (50), 46651–46657.

(33) Shimada, H.; Yamaguchi, T.; Kishimoto, H.; Sumi, H.; Yamaguchi, Y.; Nomura, K.; Fujishiro, Y. Nanocomposite Electrodes for High Current Density over 3 A Cm−2 in Solid Oxide Electrolysis Cells. *Nat. Commun.* **2019**, *10* (1), 5432.

(34) Lee, Y. H.; Ren, H.; Wu, E. A.; Fullerton, E. E.; Meng, Y. S.; Minh, N. Q. All-Sputtered, Superior Power Density Thin-Film Solid Oxide Fuel Cells with a Novel Nanofibrous Ceramic Cathode. *Nano Lett.* **2020**, *20* (5), 2943–2949.

(35) Develos-Bagarinao, K.; Ishiyama, T.; Kishimoto, H.; Shimada, H.; Yamaji, K. Nanoengineering of Cathode Layers for Solid Oxide Fuel Cells to Achieve Superior Power Densities. *Nat. Commun.* **2021**, *12* (1), 3979.

(36) Shin, J. F.; Xu, W.; Zanella, M.; Dawson, K.; Savvin, S. N.; Claridge, J. B.; Rosseinsky, M. J. Self-Assembled Dynamic Perovskite Composite Cathodes for Intermediate Temperature Solid Oxide Fuel Cells. *Nat. Energy* **2017**, *2* (3), 16214.

(37) MacManus-Driscoll, J. L.; Zerrer, P.; Wang, H.; Yang, H.; Yoon, J.; Fouchet, A.; Yu, R.; Blamire, M. G.; Jia, Q. Strain Control and Spontaneous Phase Ordering in Vertical Nanocomposite Heteroepitaxial Thin Films. *Nat. Mater.* **2008**, *7* (4), 314–320.

(38) Chen, A.; Su, Q.; Han, H.; Enriquez, E.; Jia, Q. Metal Oxide Nanocomposites: A Perspective from Strain, Defect, and Interface. *Adv. Mater.* **2019**, *31* (4), 1803241.

(39) Lee, S.; Zhang, W.; Khatkhatay, F.; Wang, H.; Jia, Q.; MacManus-Driscoll, J. L. Ionic Conductivity Increased by Two Orders of Magnitude in Micrometer-Thick Vertical Yttria-Stabilized ZrO $_2$ Nanocomposite Films. *Nano Lett.* **2015**, *15* (11), 7362–7369.

(40) Ma, W.; Kim, J. J.; Tsvetkov, N.; Daio, T.; Kuru, Y.; Cai, Z.; Chen, Y.; Sasaki, K.; Tuller, H. L.; Yildiz, B. Vertically Aligned Nanocomposite La $_{0.8}$ Sr $_{0.2}$ CoO $_3$ /(La $_{0.5}$ Sr $_{0.5}$) $_2$ CoO $_4$ Cathodes – Electronic Structure, Surface Chemistry and Oxygen Reduction Kinetics. *J. Mater. Chem. A* **2015**, *3* (1), 207–219.

(41) Baiutti, F.; Chiabrera, F.; Acosta, M.; Diercks, D.; Parfitt, D.; Santiso, J.; Wang, X.; Cavallaro, A.; Morata, A.; Wang, H.; Chroneos, A.; MacManus-Driscoll, J.; Tarancon, A. A High-Entropy Manganite in an Ordered Nanocomposite for Long-Term Application in Solid Oxide Cells. *Nat. Commun.* **2021**, *12* (1), 2660.

(42) Sirvent, J. D. D.; Carmona, A.; Rapenne, L.; Chiabrera, F.; Morata, A.; Burriel, M.; Baiutti, F.; Tarancón, A. Nanostructured La $_{0.75}$ Sr $_{0.25}$ Cr $_{0.5}$ Mn $_{0.5}$ O $_{3}$ –Ce $_{0.8}$ Sm $_{0.2}$ O $_{2}$ Heterointerfaces as All-Ceramic Functional Layers for Solid Oxide Fuel Cell Applications. *ACS Appl. Mater. Interfaces* **2022**, *14* (37), 42178–42187.

(43) Yoon, J.; Cho, S.; Kim, J.-H.; Lee, J.; Bi, Z.; Serquis, A.; Zhang, X.; Manthiram, A.; Wang, H. Vertically Aligned Nanocomposite Thin Films as a Cathode/Electrolyte Interface Layer for Thin-Film Solid Oxide Fuel Cells. *Adv. Funct. Mater.* **2009**, *19* (24), 3868–3873.

(44) Machado, M.; Baiutti, F.; Bernadet, L.; Morata, A.; Nuñez, M.; Ouweltjes, J. P.; Fonseca, F. C.; Torrell, M.; Tarancón, A. Functional Thin Films as Cathode/Electrolyte Interlayers: A Strategy to Enhance the Performance and Durability of Solid Oxide Fuel Cells. *J. Mater. Chem. A* **2022**, *10* (33), 17317–17325.

(45) Wold, A.; Ward, R. Perowskite-Type Oxides of Cobalt, Chromium and Vanadium with Some Rare Earth Elements. *J. Am. Chem. Soc.* **1954**, *76* (4), 1029–1030.

(46) Artini, C.; Pani, M.; Carnasciali, M. M.; Buscaglia, M. T.; Plaisier, J. R.; Costa, G. A. Structural Features of Sm- and Gd-Doped Ceria Studied by Synchrotron X-Ray Diffraction and μ-Raman Spectroscopy. *Inorg. Chem.* **2015**, *54* (8), 4126–4137.

(47) Kim, D.-J. Lattice Parameters, Ionic Conductivities, and Solubility Limits in Fluorite-Structure MO2 Oxide [M = Hf4+, Zr4+, Ce4+, Th4+, U4+] Solid Solutions. *J. Am. Ceram. Soc.* **1989**, *72* (8), 1415–1421.

(48) Sasaki, S.; Fujino, K.; Takéuchi, Y. X-Ray Determination of Electron-Density Distributions in Oxides, MgO, MnO, CoO, and NiO, and Atomic Scattering Factors of Their Constituent Atoms. *Proc. Jpn. Acad. Ser. B* **1979**, *55* (2), 43–48.

(49) Ishii, A.; Nemoto, N.; Yamaguchi, M.; Kobayashi, K.; Oikawa, I.; Takano, A.; Hitomi, T.; Hayashi, N.; Takamura, H. Key Role of Interfacial Cobalt Segregation in Stable Low-Resistance Composite Oxygen-Reducing Electrodes. *ACS Appl. Mater. Interfaces* **2023**, *15* (29), 34809–34817.

(50) Gault, B., Chiaramonti, A., Cojocaru-Mirédin, O., Stender P., Dubosq R., Freysoldt C., Makineni S. K., Li T., Moody M., Cairney J. H. Atom probe tomography. *Nat Rev Methods Primers* **2021**, 51 (1).

(51) Huang, J.; MacManus-Driscoll, J. L.; Wang, H. New Epitaxy Paradigm in Epitaxial Self-Assembled Oxide Vertically Aligned Nanocomposite Thin Films. *J. Mater. Res.* **2017**, *32* (21), 4054–4066.

(52) Adler, S. B. Mechanism and Kinetics of Oxygen Reduction on Porous La12xSrxCoO32d Electrodes. *Solid State Ion.* **1998**.

(53) Schmid, A.; Rupp, G. M.; Fleig, J. How To Get Mechanistic Information from Partial Pressure-Dependent Current–Voltage Measurements of Oxygen Exchange on Mixed Conducting Electrodes. *Chem. Mater.* **2018**, *30* (13), 4242–4252.

(54) Koohfar, S.; Ghasemi, M.; Hafen, T.; Dimitrakopoulos, G.; Kim, D.; Pike, J.; Elangovan, S.; Gomez, E. D.; Yildiz, B. Improvement of Oxygen Reduction Activity and Stability on a Perovskite Oxide Surface by Electrochemical Potential. *Nat. Commun.* **2023**, *14* (1), 7203.

(55) Cook, K.; Wrubel, J.; Ma, Z.; Huang, K.; Jin, X. Modeling Electrokinetics of Oxygen Electrodes in Solid Oxide Electrolyzer Cells. *J. Electrochem. Soc.* **2021**, *168* (11), 114510.

(56) Van Der Heide, P. A. W. Systematic X-Ray Photoelectron Spectroscopic Study of La1?XSrx-Based Perovskite-Type Oxides. *Surf. Interface Anal.* **2002**, *33* (5), 414–425.

(57) Yang, Y.; Bao, H.; Ni, H.; Ou, X.; Wang, S.; Lin, B.; Feng, P.; Ling, Y. A Novel Facile Strategy to Suppress Sr Segregation for High-Entropy Stabilized La0·8Sr0·2MnO3-δ Cathode. *J. Power Sources* **2021**, *482*, 228959.

(58) Lin, Z.; Ma, B.; Chen, Z.; Zhou, Y. Nanostructured Spinel High-Entropy Oxide (Fe0.2Mn0.2Co0.2Ni0.2Zn0.2)3O4 as a Potential Cathode for Solid Oxide Fuel Cells. *Ceram. Int.* **2023**, *49* (14), 23057–23067.

(59) Morales, M.; Pesce, A.; Slodczyk, A.; Torrell, M.; Piccardo, P.; Montinaro, D.; Tarancón, A.; Morata, A. Enhanced Performance of Gadolinia-Doped Ceria Diffusion Barrier Layers Fabricated by Pulsed Laser Deposition for Large-Area Solid Oxide Fuel Cells. *ACS Appl. Energy Mater.* **2018**, *1* (5), 1955–1964.

(60) Bernadet, L.; Segura-Ruiz, J.; Yedra, L.; Estrade, S.; Peiró, F.; Montinaro, D.; Torrell, M.; Morata, A.; Tarancón, A. Enhanced Diffusion Barrier Layers for Avoiding Degradation in SOFCs Aged for 14000 h during 2 Years. *J. Power Sources* **2023**, *555*, 232400.

(61) Gao, Z.; Zenou, V. Y.; Kennouche, D.; Marks, L.; Barnett, S. A. Solid Oxide Cells with Zirconia/Ceria Bi-Layer Electrolytes Fabricated by Reduced Temperature Firing. *J. Mater. Chem. A* **2015**, *3* (18), 9955–9964.

(62) Lu, Z.; Hardy, J.; Templeton, J.; Stevenson, J.; Fisher, D.; Wu, N.; Ignatiev, A. Performance of Anode-Supported Solid Oxide Fuel Cell with Thin Bi-Layer Electrolyte by Pulsed Laser Deposition. *J. Power Sources* **2012**, *210*, 292–296.

(63) Wang, H.; Zhang, W.; Guan, K.; Wei, Z.; Meng, J.; Meng, J.; Liu, X. Enhancing Activity and Durability of A-Site-Deficient ($La_{0.6}Sr_{0.4})_{0.95}Co_{0.2}Fe_{0.8}O_{3-\delta}$ Cathode by Surface Modification with $PrO_{2-\delta}$ Nanoparticles. *ACS Sustain. Chem. Eng.* **2020**, *8* (8), 3367–3380.

(64) Chang, J.-C.; Lee, M.-C.; Yang, R.-J.; Chang, Y.-C.; Lin, T.-N.; Wang, C.-H.; Kao, W.-X.; Lee, L.-S. Fabrication and Characterization of Sm0.2Ce0.8O2−δ–Sm0.5Sr0.5CoO3−δ Composite Cathode for Anode Supported Solid Oxide Fuel Cell. *J. Power Sources* **2011**, *196* (6), 3129–3133.

(65) Fan, H.; Liu, Z.; Wu, Y.; Wang, Q.; Yang, J.; Guan, W.; Han, L.; Wang, J. Electrochemical Performance of $La_{0.6}Sr_{0.4}CoO_{3-\delta}$–$Ce_{0.9}Gd_{0.1}O_{1.95}$ Composite Cathode for IT-SOFCs. *Int. J. Appl. Ceram. Technol.* **2024**, *21* (1), 289–298.

(66) Kim, D. H.; Yang, S.; Kwon, D.; Ji, H.; Son, J.; Shim, J. H. Improved Strontium Segregation Suppression of Lanthanum Strontium Cobalt Oxide Cathode via Chemical Etching and Atomic Layer Deposition. *Int. J. Energy Res.* **2022**, *46* (9), 12467–12475.

(67) Shin, S. S.; Kim, J. H.; Bae, K. T.; Lee, K.-T.; Kim, S. M.; Son, J.-W.; Choi, M.; Kim, H. Multiscale Structured Low-Temperature Solid Oxide Fuel Cells with 13 W Power at 500 °C. *Energy Environ. Sci.* **2020**, *13* (10), 3459–3468.

(68) Zheng, Y.; Li, Q.; Chen, T.; Wu, W.; Xu, C.; Wang, W. G. Comparison of Performance and Degradation of Large-Scale Solid Oxide Electrolysis Cells in Stack with Different Composite Air Electrodes. *Int. J. Hydrog. Energy* **2015**, *40* (6), 2460–2472.

(69) Chen, M.; Sun, X.; Chatzichristodoulou, C.; Koch, S.; Hendriksen, P. V.; Mogensen, M. B. Thermoneutral Operation of Solid Oxide Electrolysis Cells in Potentiostatic Mode. *ECS Trans.* **2017**, *78* (1), 3077–3088.

(70) Bernadet, L.; Buzi, F.; Baiutti, F.; Segura-Ruiz, J.; Dolado, J.; Montinaro, D.; Torrell, M.; Morata, A.; Tarancón, A. Thickness Effect of Thin-Film Barrier Layers for Enhanced Long-Term Operation of Solid Oxide Fuel Cells. *APL Energy* **2023**, *1* (3), 036101.